Synthesis and Characterization of Monolayer-Capped PtVFe Nanoparticles with Controllable Sizes and Composition

Jin Luo,[†] Li Han,[†] Nancy N. Kariuki,[†] Lingyan Wang,[†] Derrick Mott,[†] Chuan-Jian Zhong,*[,†] and T. He*[,‡]

Department of Chemistry, State University of New York at Binghamton, Binghamton, New York 13902, and Honda Research Institute USA, Inc., 1381 Kinnear Road, Columbus, Ohio 43212

Received April 18, 2005. Revised Manuscript Received August 12, 2005

The ability to control the size and composition of metal nanoparticles is essential in preparing binary or ternary catalysts. This paper reports the results of an investigation of a core−shell synthesis protocol for the preparation of monolayer-capped ternary platinum−vanadium−iron (PtVFe) nanoparticles with a few nanometers in core sizes. Our approach involves the use of metal precursors, capping agents, and reducing agents in controllable ratios for the reaction in a single organic phase. By manipulating the relative concentration ratios of the metal precursors such as platinum acetylacetonate, vanadyl acetylacetonate, and iron pentacarbonyl, and capping agents such as oleic amine and oleic acids, the core−shell type nanoparticles in which the nanocrystal PtVFe cores are encapsulated with a shell of mixed amine/acid monolayer have been successfully synthesized. The average diameters of the nanocrystalline cores are well controlled between 1.4 and 3.5 nm with high monodispersity (±0.3−0.5 nm). The chemical composition of the nanocrystalline cores is shown to be effectively controllable in the range of Pt (20−40%), V (10−40%), and Fe (40−70%) by manipulating the feeding ratios of the metal precursors. The results of characterizations using TEM, DCP-AES, XRD, FTIR, and TGA techniques are discussed, along with their implications to the exploration of the nanoparticles as fuel cell catalysts.

Introduction

The preparation of platinum (Pt)-group catalysts, especially Pt alloyed with other transition metals, has been extensively studied for fuel cell catalytic reactions.[1−6] Traditional approaches to preparing supported nanoparticle catalysts involve coprecipitation, deposition-precipitation, ion-exchange, impregnation, successive reduction, and calcination, etc. These methods have been widely used for preparing noble metal catalysts on support materials.[7] While a variety of supported Pt-group binary or ternary catalysts have been prepared by traditional methods,[6−15] the ability to control the size and composition is limited due to the propensity of aggregation of metals at the nanoscale. One of the most challenging areas is the development of abilities to control size and composition in the 1−10 nm size range. As the size of a particle approaches this size range, both surface area-to-volume ratio and surface-to-bulk atom ratio dramatically increase. This increase leads to a number of important attributes, including high surface concentrations of corner and edge atoms, low coordination numbers of surface atoms, and unique electronic properties (e.g., quantum transition). It is in this size range over which metal nanoparticles undergo a transition from atomic to metallic properties. Moreover, possible synergistic effect could be produced by binary or ternary compositions, involving the suppression of adsorbed poisonous species and the change in electronic band structure to modify the strength of the chemical adsorption. This property is highly dependent on the atomic arrangement of different components on the surface.

Among many emerging approaches to the preparation of nanoparticles or nanostructures, one particular class of nanoparticles with core−shell type structures is beginning to attract interest for addressing some of the challenges in nanoscale catalyst preparation.[16−19] The core−shell type

* To whom correspondence should be addressed. E-mail: cjzhong@binghamton.edu (C.J.Z.); the@oh.hra.com (T.H.).
[†] State University of New York at Binghamton.
[‡] Honda Research Institute USA, Inc.

(1) Spendelow, J. S.; Wieckowski, A. *Phys. Chem. Chem. Phys*. **2004**, *6*, 5094.
(2) Bonnemann, H.; Nagabhushana, K. S. *J. New Mater. Electrochem. Syst*. **2004**, *7*, 93.
(3) Litster, S.; McLean, G. *J. Power Sources* **2004**, *130*, 61.
(4) Antolini, E. *Mater. Chem. Phys.* **2003**, *78*, 563.
(5) Rao, C. R. K.; Trivedi, D. C. *Coord. Chem. Rev.* **2005**, *249*, 613.
(6) Yang, H.; Vogel, W.; Lamy, C.; Alonso-Vante, N. *J. Phys. Chem. B* **2004**, *108*, 11024.
(7) Klabunde, K. J., Ed. *Nanoscale Materials in Chemistry*; John Wiley & Sons: New York, 2001.
(8) Feldheim, D. L., Foss, C. A., Jr., Eds. *Metal Nanoparticles: Synthesis, Characterization, and Applications*; Marcel Dekker: New York, 2002.
(9) Waszczuk, P.; Lu, G. Q.; Wieckowski, A.; Lu, C.; Rice, C.; Masel, R. I. *Electrochim. Acta* **2002**, *47*, 3637.
(10) Park, K. W.; Choi, J. H.; Kwon, B. K.; Lee, S. A.; Sung, Y. E.; Ha, H. Y.; Hong, S. A.; Kim, H.; Wieckowski, A. *J. Phys. Chem. B* **2002**, *106*, 1869.
(11) Schmidt, T. J.; Gasteiger, H. A.; Behm, R. J. *Electrochem. Commun.* **1999**, *1*, 1.
(12) Paulus, U. A.; Wokaun, A.; Scherer, G. G.; Schmidt, T. J.; Stamenkovic, V.; Radmilovic, V.; Markovic, N. M.; Ross, P. N. *J. Phys. Chem. B* **2002**, *106*, 4181.
(13) Raja, R.; Khimyak, T.; Thomas, J. M.; Hermans, S.; Johnson, B. F. G. *Angew. Chem., Int. Ed*. **2001**, *40*, 4638.
(14) Jones, F. E.; Milne, S. B.; Gurau, B.; Smotkin, E. S.; Stock, S. R.; Lukehart, C. M. *J. Nanosci. Nanotechnol*. **2002**, *2*, 81.
(15) Dickinson, A. J.; Carrette, L. P. L.; Collins, J. A.; Friedrich, K. A.; Stimming, U. *Electrochim. Acta* **2002**, *47*, 3733.
(16) Brust, M.; Walker, M.; Bethell, D.; Schiffrin, D. J.; Whyman, R. *J. Chem. Soc., Chem. Commun*. **1994**, 801.

10.1021/cm0508219 CCC: $30.25
Published on Web 09/23/2005

nanomaterials can be broadly defined as core and shell of different matters in close interaction, including inorganic/organic and inorganic/inorganic combinations.[16−23] The core−shell type nanoparticles serve as building blocks toward catalytic materials by taking advantage of diverse attributes, including size monodispersity, processability, solubility, stability, self-assembly capability, and controllable electronic properties. This paper focuses on the core−shell preparation of ternary metal nanocrystal cores capped with organic monolayer shells.

There has been an increasing volume of studies in recent years aimed at synthesizing metal nanoparticles in the presence of organic capping agents.[18,21−32] While the synthesis of monometallic nanoparticles such as gold, silver, platinum, and palladium has extensively been studied using molecular encapsulation-based synthesis methods (e.g., two-phase protocol), relatively limited studies of bi- or tri-metallic nanoparticles have been reported using such synthetic methods.[18,30−33] With molecular encapsulation in both two-phase and single-phase protocols, we have recently demonstrated the ability to synthesize size- and composition-controllable binary (e.g., gold−silver[34] and gold−platinum[35−37]) nanoparticles, which show promises for further expansion to many other multicomponent nanoparticle systems. In the present paper, we report the results of an investigation of the core−shell method in a single phase for the synthesis of ternary PtVFe nanoparticles with average sizes of a few nanometers. The approach involves the use of metal precursors, capping agents, and reducing agents in controllable ratios in a single organic phase. This approach is an expansion of an elegant protocol previously reported for the synthesis of binary PtFe nanoparticles with organic monolayer encapsulation.[30] By manipulating the relative concentrations of the three metal precursors, the core−shell type nanoparticles in which the nanocrystal PtVFe cores are encapsulated with a monolayer shell of amines/acids were successfully synthesized. The average diameters of the nanocrystal cores were well controlled between 1.4 and 3.5 nm with high monodispersity. The composition of the ternary nanocrystalline cores is controlled by manipulating the feeding ratios of the metal precursors used for the synthesis. The correlation between the composition of the nanoparticles and the feeding ratios of the metal precursors is also delineated. The size- and composition-controlled synthesis of the PtVFe nanoparticles is, to our knowledge, the first example demonstrating the viability of one-pot synthesis of core−shell type ternary metal nanoparticles.

Scheme 1. A Schematic Illustration of the Synthesis of PtVFe Nanoparticles

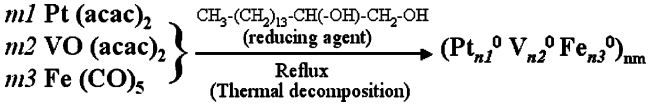

Experimental Section

Chemicals. Platinum(II) acetylacetonate ($Pt(acac)_2$, 97%), vanadium(III) acetylacetonate ($V(acac)_3$, 97%), iron pentacarbonyl ($Fe(CO)_5$), 1,2-hexadecanediol ($CH_3-(CH_2)_{13}-CH(-OH)-CH_2-OH$, 90%), octyl ether ($[CH_3(CH_2)_7]_2O$, 99%), oleylamine ($CH_3-(CH_2)_7CH=CH(CH_2)_8NH_2$, 70%), and oleic acid ($CH_3(CH_2)_7CH=CH(CH_2)_7COOH$, 99+%) were purchased from Aldrich and used as received. Vanadyl acetylacetonate ($VO(acac)_2$, 97%) was purchased from Lancaster Synthesis Inc. and was used as received. Other chemicals such as ethanol and hexane were purchased from Fisher.

Synthesis Protocols. The general synthesis of PtVFe nanoparticles involved the use of three metal precursors, $Pt^{II}(acac)_2$, $V^{IV}O(acac)_2$, and $Fe^0(CO)_5$, in controlled molar ratios. These metal precursors were dissolved in an octyl ether solvent. A mixture of oleylamine and oleic acid was also dissolved in the solution and used as capping agent. 1,2-Hexadecanediol was used as a reducing agent for the reduction of the Pt- and V-precursors, and elevated temperature was used to initiate the thermal decomposition of the Fe-precursor. The general reaction for the synthesis of the (oleylamine/oleic acid)-capped PtVFe nanoparticles involves thus a combination of thermal decomposition and reduction reactions, as illustrated in Scheme 1. Both $Pt^{II}(acac)_2$ and $V^{IV}O(acac)_2$ are reduced to Pt^0 and V^0 by 1,2-hexadecanediol, whereas $Fe^0(CO)_5$ is thermally decomposed into Fe^0. The composition of the $Pt^0_{n1}V^0_{n2}Fe^0_{n3}$ nanoparticles, where *n1*, *n2*, and *n3* represent the atomic percentages of each metal, is controlled by the feeding ratio of the metal precursors, which is expressed in molar percentages (*m1*, *m2*, and *m3*). The nanoparticle product is soluble in the reaction solution and can be collected by precipitation method. Possible byproducts include $CH_2-(CH_2)_{13}-CH(-OH)-CH(=O)$ (aldehyde), $CH_2-(CH_2)_{13}-CH(-OH)-COOH$ (carboxylic acid), acac, and CO, which were soluble in the solvent and were discarded after precipitating out the nanoparticles.

PtVFe nanoparticles of different compositions were synthesized by manipulating the relative concentrations of metal precursors such as platinum(II) acetylacetonate, vanadyl acetylacetonate, and iron pentacarbonyl, and capping agents such as oleylamine and oleic acid. In a typical procedure for the synthesis of $Pt_{33}V_{14}Fe_{53}$,[38] for

(17) Schmid, G.; Maihack, V.; Lantermann, F.; Peschel, S. *J. Chem. Soc., Dalton Trans*. **1996**, 589.
(18) Paulus, U. A.; Endruschat, U.; Feldmeyer, G. J.; Schmidt, T. J.; Bonnemann, H.; Behm, R. J. *J. Catal.* **2000**, *195*, 383.
(19) Templeton, A. C.; Wuelfing, W. P.; Murray, R. W. *Acc. Chem. Res*. **2000**, *33*, 27 and references therein.
(20) Whetten, R. L.; Khoury, J. T.; Alvarez, M. M.; Murthy, S.; Vezmar, I.; Wang, Z. L.; Stephens, P. W.; Cleveland, C. L.; Luedtke, W. D.; Landman, U. *Adv. Mater*. **1996**, *8*, 428.
(21) El-Sayed, M. A. *Acc. Chem. Res*. **2001**, *34*, 257.
(22) Kiely, C. J.; Fink, J.; Zheng, J. G.; Brust, M.; Bethell, D.; Schiffrin, D. J. *Adv. Mater*. **2000**, *12*, 640.
(23) Zhong, C. J.; Maye, M. M. *Adv. Mater*. **2001**, *13*, 1507.
(24) Caruso, F. *Adv. Mater*. **2001**, *13*, 11 and references therein.
(25) Schneider, J. J. *Adv. Mater*. **2001**, *13*, 529.
(26) Schärtl, W. *Adv. Mater*. **2000**, *12*, 1899.
(27) Storhoff, J. J.; Mirkin, C. A. *Chem. Rev*. **1999**, *99*, 1849.
(28) Mbindyo, J. K. N.; Reiss, B. D.; Martin, B. R.; Keating, C. D.; Natan, M. J.; Mallouk, T. E. *Adv. Mater*. **2001**, *13*, 249.
(29) Crooks, R. M.; Zhao, M. Q.; Sun, L.; Chechik, V.; Yeung, L. K. *Acc. Chem. Res*. **2001**, *34*, 181.
(30) Sun, S. H.; Murray, C. B.; Weller, D.; Folks, L.; Moser, A. *Science* **2000**, *287*, 1989.
(31) Sun, S. H.; Fullerton, E. E.; Weller, D.; Murray, C. B. *IEEE Trans. Magn*. **2001**, *37*, 1239.
(32) Chen, M.; Nikles, D. E. *Nano Lett.* **2002**, *2*, 211.
(33) Hostetler, M. J.; Zhong, C. J.; Yen, B. K. H.; Anderegg, J.; Gross, S. M.; Evans, N. D.; Porter, M. D.; Murray, R. W. *J. Am. Chem. Soc*. **1998**, *120*, 9396.
(34) Kariuki, N. N.; Luo, J.; Maye, M. M.; Hassan, S. A.; Menard, T.; Naslund, H. R.; Lin, Y.; Wang, C.; Engelhard, M. H.; Zhong, C. J. *Langmuir* **2004**, *20*, 11240.
(35) Maye, M. M.; Kariuki, N. N.; Luo, J.; Han, L.; Njoki, P.; Wang, L.; Lin, Y.; Naslund, H. R.; Zhong, C. J. *Gold Bull.* **2004**, *37*, 217.
(36) Luo, J.; Maye, M. M.; Kariuki, N. N.; Wang, L.; Njoki, P.; Lin, Y.; Schadt, M.; Naslund, H. R.; Zhong, C. J. *Catal. Today* **2005**, *99*, 291.
(37) Luo, J.; Maye, M. M.; Petkov, V.; Kariuki, N. N.; Wang, L.; Njoki, P.; Mott, D.; Lin, Y.; Zhong, C. J. *Chem. Mater*. **2005**, *17*, 3086.

Scheme 2. A Schematic Illustration of the Core−Shell Structure of PtVFe Nanoparticles (Oleylamine: $CH_3(CH_2)_7CH{=}CH(CH_2)_8NH_2$; Oleic acid: $CH_3(CH_2)_7CH{=}CH(CH_2)_7CO_2H$)

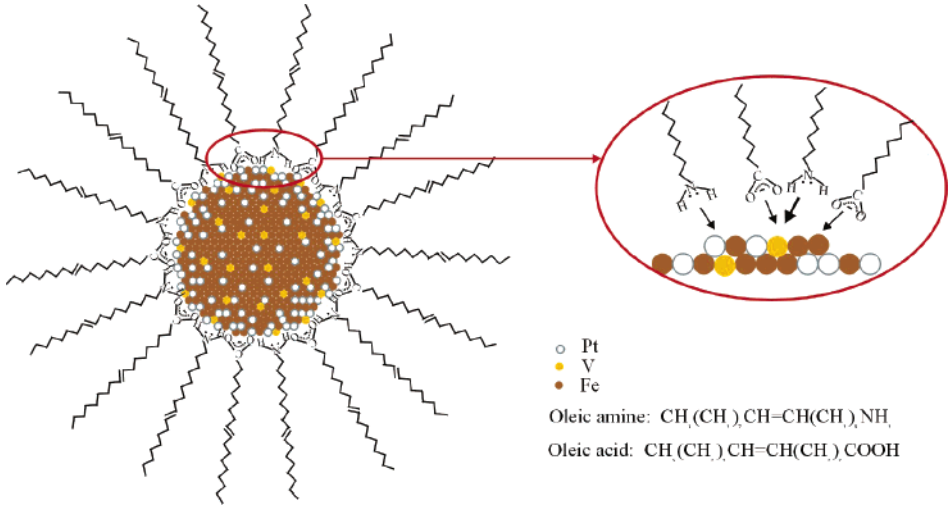

example, 0.50 g of 1,2-hexadecanediol (1.74 mmol), 0.15 g of vanadyl acetylacetonate ($VO(acac)_2$, 0.55 mmol), 0.40 g of platinum acetylacetonate ($Pt(acac)_2$, 0.99 mmol), and 60 mL of octyl ether were added to a three-neck 250 mL flask under stirring. The solution was purged with N_2 and heated to 105 °C. The solution appeared as a dark green color. At this temperature and under N_2 atmosphere, 0.3 mL of oleylamine (0.64 mmol), 0.3 mL of oleic acid (0.94 mmol), and 0.3 mL of $Fe(CO)_5$ (2.28 mmol) were added into the solution. N_2 purging was stopped, and the solution was kept under N_2. The mixture was heated to 270 °C and refluxed for 40 min. The solution appeared as a black color. After the reaction mixture was allowed to cool to room temperature, the solution was transferred to a large flask under ambient environment. The product was precipitated by adding ethanol (∼200 mL). The yellow-brown supernatant was discarded. The black precipitate was dispersed in hexane (∼100 mL) in the presence of oleic acid (∼0.15 mL) and oleylamine (∼0.15 mL) and precipitated out by adding ethanol (∼200 mL) and centrifuging. The product was redispersed in hexane (∼100 mL), centrifuged to remove any unsolved precipitation, precipitated out by adding ethanol (∼200 mL), and dried under N_2. The nanoparticle product was redispersed in hexane and stored under N_2.

We also note that PtVFe nanoparticles could also be synthesized using different metal precursors. For example, $V(acac)_3$ was used to replace $VO(acac)_2$, and $Fe(acac)_2$ was used to replace $Fe(CO)_5$. Similar results were obtained but with subtle differences in composition or particle sizes.[39,40]

Measurements. *Transmission Electron Microscopy.* Transmission electron microscopy (TEM) was performed on a Hitachi H-7000 electron microscope (100 kV). For TEM measurements, nanoparticle samples were diluted in hexane solution and were drop-cast onto a carbon-coated copper grid followed by solvent evaporation in air at room temperature.

Direct Current Plasma-Atomic Emission Spectroscopy (DCP-AES). The composition was analyzed using the direct current plasma-atomic emission spectroscopy, which was performed using an ARL Fisons SS-7 Direct Current Plasma-Atomic Emission spectrometer. Measurements were made on emission peaks at 265.95, 309.31, and 259.94 nm for Pt, V, and Fe, respectively. The nanoparticle samples were dissolved in concentrated aqua regia, and then diluted to concentrations in the range of 1−50 ppm for analysis. Calibration curves were made from dissolved standards with concentrations from 0 to 50 ppm in the same acid matrix as the unknowns. Detection limits, based on three standard deviations of the background intensity, are 0.02, 0.002, and 0.005 ppm for Pt, V, and Fe. Standards and unknowns were analyzed 10 times each for 3 s counts. Instrument reproducibility, for concentrations greater than 100 times the detection limit, results in $<\pm 2\%$ error.

Thermogravimetric Analysis (TGA). Thermogravimetric analysis was performed on a Perkin-Elmer Pyris 1-TGA for determining the weight of organic shell. Typical samples weighed ∼4 mg and were heated in a platinum pan. Samples were heated in 20% O_2 at a rate of 10 °C/min.

X-ray Powder Diffraction (XRD). The products were identified by powder X-ray diffraction. Powder diffraction patterns were recorded on a scintag XDS 2000 $\theta-\theta$ powder diffractometer equipped with a Ge(Li) solid-state detector (Cu Kα radiation). The data were collected from $2\theta = 5°$ to 90° at a scan rate of 0.02° per step and 5 s per point.

Fourier Transform Infrared (FTIR). FTIR spectra were acquired on a Nicolet 760 ESP FT-IR spectrometer that was purged with boil-off from liquid N_2. The spectrometer was equipped with a liquid nitrogen-cooled HgCdTe detector. The nanoparticle powder sample was mixed with KBr powder and ground into fine powders. The powders were pressed into pellet at 15 000 psi. The nanoparticle samples were dropped on the Si-wafers and dried by N_2. The transmission IR spectra were collected over the range of 400−4000 cm^{-1}.

Results and Discussion

As illustrated in Scheme 2, the structure of our PtVFe nanoparticles involves two parts, the ternary nanocrystal core and the organic capping monolayer shell. It is important to note that each part of the structure consists of multiple components. There are clearly three basic questions that must be addressed: (1) What are the average size and monodis-

(38) The chemical composition of PtVFe nanoparticles reported here is derived from the core−shell synthesis protocol. For detailed information about the design of this ternary composition as fuel cell electrocatalyst, see: Giaquinta, D. M.; Gorer, A.; Devenney, M.; He, T.; Oyanagi, H.; Strasser, P.; Fan, Q.; Chondroudis, K. "Platinum−Vanadium−Iron fuel cell electrocatalyst", World Patent Application filed (5/19/2004).

(39) Zhong, C. J.; Luo, J.; Maye, M. M.; Han, L.; Kariuki, N. N.; He, T. "Core−shell synthesis of carbon-supported alloy nanoparticles catalyst", U.S. Patent Application filed (4/22/2004).

(40) He, T.; Zhong, C. J.; Luo, J.; Maye, M. M.; Han, L.; Kariuki, N. N.; Wang, L. "Metal and alloy nanoparticles and synthesis methods thereof", U.S. Patent Application filed (9/17/2004).

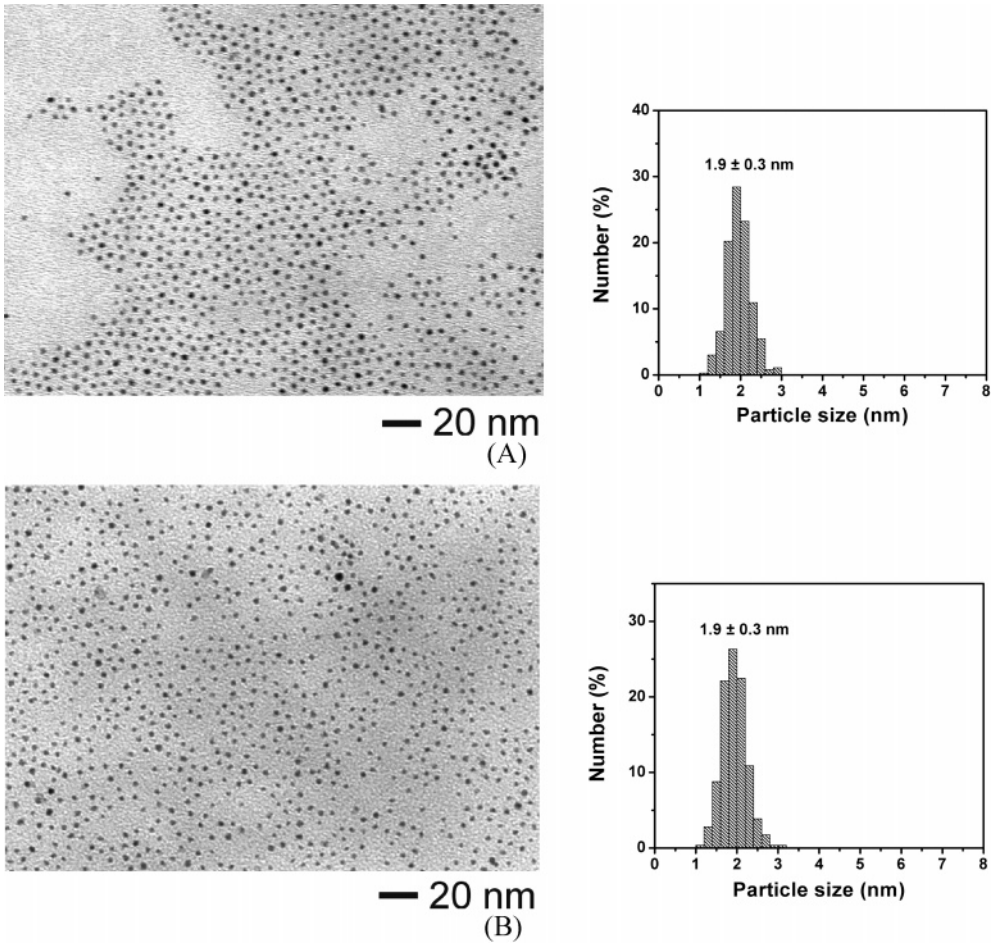

Figure 1. TEM micrographs for two samples of ternary nanoparticles. (A) $Pt_{32}V_{13}Fe_{55}$; (B) $Pt_{33}V_{14}Fe_{53}$.

persity of the nanoparticles? (2) Can the composition of metals in the ternary nanocrystal core be controlled? (3) What is the makeup of the organic monolayer shell? To address these questions, we have carried out a series of characterizations using a number of techniques, including TEM, DCP-AES, FTIR, and TGA.

The focus of these characterizations is the detailed understanding of the core−shell size, composition, and structure. The discussions of the experimental results are divided into three sections. In the first section, the results obtained for the characterization of size and morphology of the PtVFe nanoparticles are described. In the second section, the data on the metal composition in the ternary nanoparticles and its correlation with the synthetic composition are discussed. The structural properties of the encapsulating monolayer shells and the relative core−shell composition are discussed in the last section.

(1) Size and Morphology. In general, the core−shell nanoparticles obtained after the cleaning treatments as described in the Experimental Section were black and waxy powders. The powders were easily dispersed in nonpolar solvents such as hexane and toluene. The nanoparticle solution displayed a dark brown color and was stable for years.

The size and morphology of the PtVFe nanoparticles were analyzed using TEM. Typically, the nanoparticle solution was cast onto a TEM grid, and the solvent was evaporated at room temperature, leaving the particles on the carbon-coated TEM grid. Figure 1 shows a representative set of TEM micrographs for two different samples of PtVFe nanoparticles, which have very similar ternary compositions ($Pt_{32}V_{13}Fe_{55}$ and $Pt_{33}V_{14}Fe_{53}$). The indicated compositions will be discussed in the next subsection. The size distributions were determined from an analysis of ∼2000 particles in the TEM images (using a computer software). In these two examples, the basic morphology of the observed nanoparticles is largely characterized by the highly faceted nanocrystal feature, which is observable by a close examination of the shapes of the individual nanocrystals. It is evident that the particle sizes are very well controlled, and the size monodispersity is very high in comparison with data reported for many other nanoparticles with similar sizes. The average size of the particles is 1.9 ± 0.3 nm for the composition range. The fact that the nanoparticles have well-defined interparticle spacing and display domains of hexagonal ordering is indicative of the encapsulation of the nanocrystal cores by organic monolayers.

PtVFe nanoparticles of a wide range of compositions (the compositions are described in the next subsection) synthesized by the synthetic protocol as described in the Experimental Section have been examined. Figure 2 shows another set of TEM images for PtVFe nanoparticles of several different compositions. While the sizes of the ternary nanoparticles varied slightly depending on the actual composition, the data demonstrated the controllability over size monodispersity.

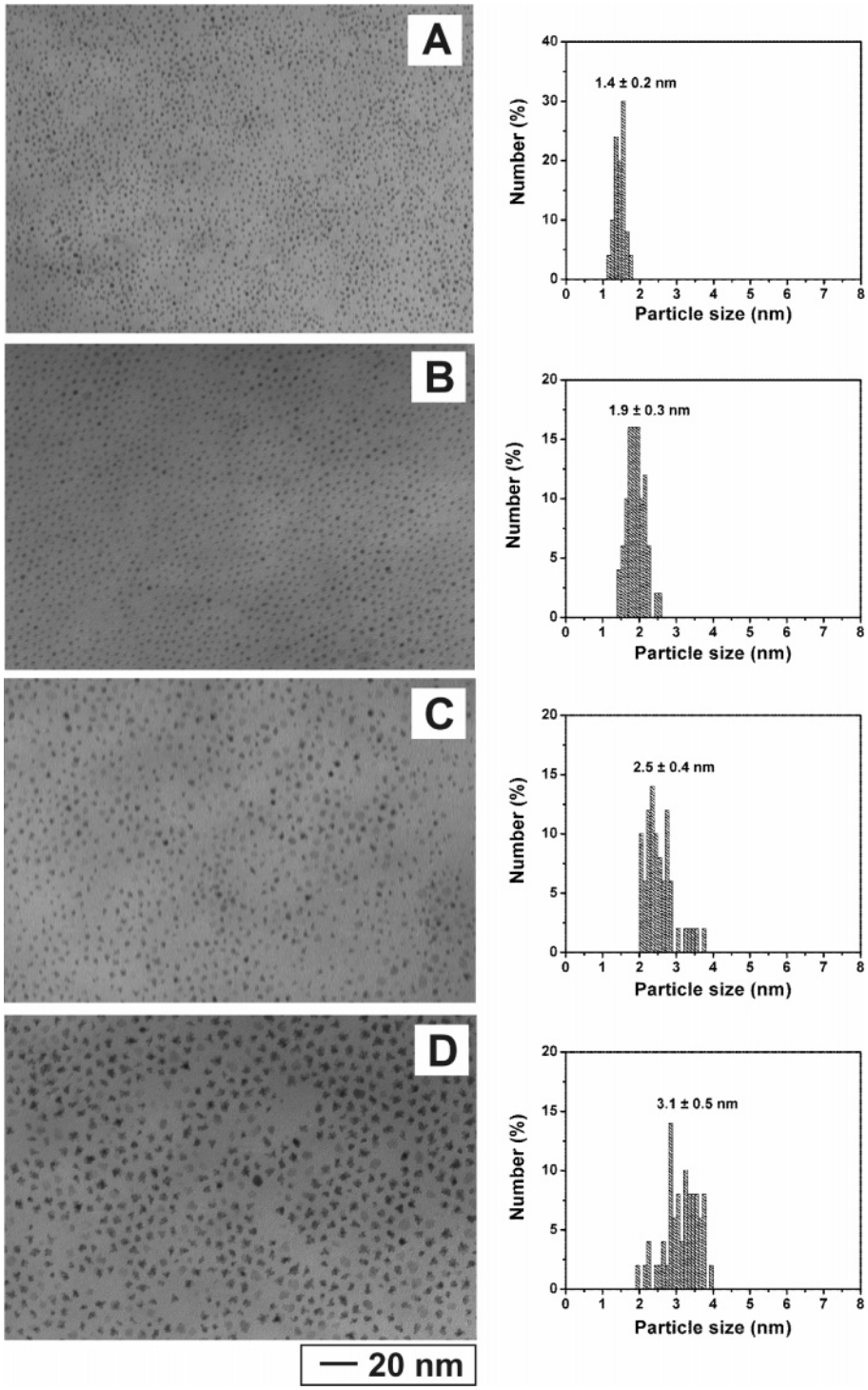

Figure 2. TEM micrographs and size distributions for a set of ternary nanoparticles with different compositions. (A) $Pt_{37}V_{16}Fe_{47}$; (B) $Pt_{32}V_{14}Fe_{54}$; (C) $Pt_{22}V_{35}Fe_{43}$; and (D) $Pt_{25}V_{35}Fe_{40}$.

Using our synthetic protocols, nanoparticles with average diameters ranging from 1.4 to 3.2 nm have been obtained. The compositions are controlled in the range from $Pt_{37}V_{16}Fe_{47}$ (A) to $Pt_{25}V_{35}Fe_{40}$ (D). The size monodispersity in most cases was very high, ranging from ±0.2 to ±0.6 nm.

(2) Composition Analysis of Nanocrystal Cores. The composition of PtVFe nanoparticles was analyzed using the DCP-AES technique. A representative set of DCP data for several PtVFe nanoparticle samples are listed in Table 1. In the table, the entries are arranged from that with the lowest Pt percentage to that with the highest Pt percentage. The

Table 1. Composition Data Determined Using DCP-AES Technique for PtVFe Nanoparticles Synthesized at Different Synthetic Feed Ratios

feed ratio	product composition[a]
$Pt_8V_{57}Fe_{35}$	$Pt_{16}V_{40}Fe_{44}$
$Pt_{10}V_{41}Fe_{49}$	$Pt_{17}V_{30}Fe_{53}$
$Pt_{10}V_{47}Fe_{43}$	$Pt_{21}V_{31}Fe_{48}$
$Pt_{10}V_{54}Fe_{36}$	$Pt_{25}V_{35}Fe_{40}$
$Pt_{12}V_{53}Fe_{35}$	$Pt_{29}V_{35}Fe_{36}$
$Pt_{23}V_{25}Fe_{52}$	$Pt_{33}V_{21}Fe_{46}$
$Pt_{26}V_{14}Fe_{60}$	$Pt_{33}V_{16}Fe_{51}$

[a] Error bar < 2%.

Table 2. DCP-AES Analytical Data for the Ternary PtVFe Nanoparticles (NP) Synthesized Using Different Precursors but the Same Synthetic Feed Ratios

feed precursors	feed ratio	NP composition[a]	particle avg. size
$Pt^{II}(acac)_2 + V^{IV}O(acac)_2 + Fe^0(CO)_5$	$Pt_{26}V_{14}Fe_{60}$	$Pt_{33}V_{14}Fe_{53}$	1.9 ± 0.3 nm
$Pt^{II}(acac)_2 + V^{III}(acac)_3 + Fe^0(CO)_5$	$Pt_{26}V_{14}Fe_{60}$	$Pt_{32}V_{13}Fe_{55}$	1.9 ± 0.3 nm
$Pt^{II}(acac)_2 + V^{IV}O(acac)_2 + Fe^{II}(acac)_2$	$Pt_{26}V_{14}Fe_{60}$	$Pt_{27}V_{11}Fe_{62}$	1.9 ± 0.5 nm

[a] Error bar < 2%.

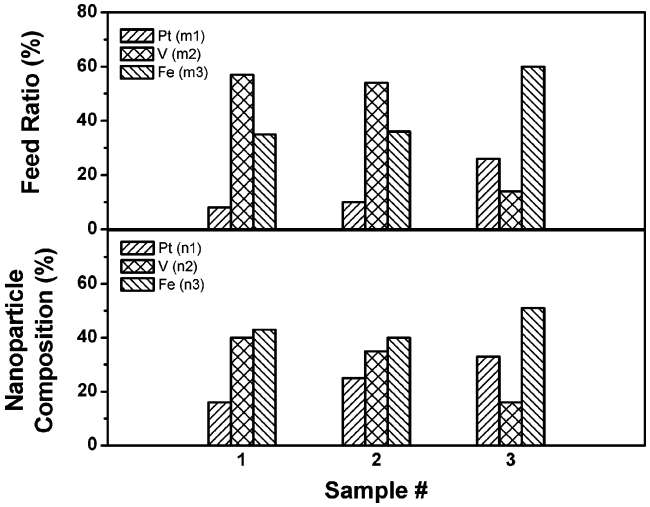

Figure 3. A graphic comparison between the feed ratio (top graph) and the nanoparticle composition (bottom graph) for three typical synthesis batches (sample no.). Note that both the feed ratio and the nanoparticle composition are expressed as % of each metal.

synthesis from at least five different batches indicated that the nanoparticle compositions were very reproducible. The error bars were <2%, which was close to the error of DCP analysis (±2%). The data in Table 1 provide a quantitative comparison between the synthetic feeding ratios and the nanoparticle composition. There are several important observations. First, the trend for the variation of the metal composition in the nanoparticles is very similar to the trend for the variation of the metal precursor ratios. In general, as the relative Pt concentration used in the synthesis increases, the relative Pt nanoparticles increase. The relative variation of V and Fe also followed similar trends. Second, the relative composition found in the nanoparticle products was not exactly the same as the feed ratios of the metal precursors used for the synthesis of nanoparticles. The difference likely reflects the thermodynamic differences between the reduction of Pt^{II} and V^{IV} to Pt^0 and V^0 and the decomposition of $Fe^0(CO)_5$ into Fe^0, and their relative driving force for atomic aggregation in forming the ternary nanoparticles.

The difference in the relative metal composition before and after synthesis can be further visualized by comparing the composition obtained for the nanoparticle products (*n1*:*n2*:*n3*) against the composition fed (*m1*:*m2*:*m3*) in the synthetic reaction (Figure 3). This comparison provides three pieces of important information about the relationship of the relative composition between the nanoparticle product and the synthetic feeding ratio. First, the increase of *m1*(Pt)% leads to an increase in *n1*(Pt)% in the nanoparticles. Second, *n2*(V)% found in the nanoparticles was less than those used in the synthetic feeding *m2*(V)% in most cases. Finally, *n3*(Fe)% found in the nanoparticles was generally quite close to those used in the synthetic feeding *m3*(Fe)%. It is apparent that the thermodynamic competition for the formation of each metal in the ternary nanoparticles is different. The reduction of $Pt(acac)_2$ seemed to be more favorable than that for $VO(acac)_2$. In addition, the reduction reactions of $Pt(acac)_2$ and $VO(acac)_2$ without $Fe(CO)_5$ occurred at a higher temperature than those in the presence of $Fe(CO)_5$. The reduction reactions ($Pt^{II} \rightarrow Pt^0$ and $V^{IV} \rightarrow V^0$) appear to be a leg behind the thermal decomposition reaction ($Fe^0(CO)_5 \rightarrow Fe^0 + CO$), probably due to a combination of kinetic and thermodynamic factors. A further study of these factors and the manipulation of the reaction temperature should allow us to develop a better correlation of the relative compositions.

Regardless of the relative composition differences, our results showed that the composition of the alloy components in the nanoparticles could be controlled by the feed ratio of the three metal precursors in the synthetic reaction solution. While the average particle size was found to show some dependence on composition, the change in particle size is relatively small.

The PtVFe nanoparticles synthesized using other metal precursors were also examined. In Table 2, the relative metal compositions found in the nanoparticle and those used in the synthesis are compared for several cases using different combinations of metal precursors. In each case, identical concentration of Pt-precursor was used, whereas the feed ratios of the metal precursors were kept the same. The variations of the metal precursors involved the use of $V(acac)_3$ to replace $VO(acac)_2$, and $Fe(acac)_2$ to replace $Fe(CO)_5$. From the first two entries in Table 2, it is clear that the nanoparticles synthesized are quite similar in terms of the ternary composition and the average particle size. This observation suggests that the reduction reaction of $V^{IV}O(acac)_2$ is effectively similar to that for $V^{III}(acac)_3$. For the use of $Fe(acac)_2$ to replace $Fe(CO)_5$ (comparing the first and the third entries in Table 2), the average particle size derived from the use of $Fe^{II}(acac)_2$ was also found to be comparable to that derived from using $Fe^0(CO)_5$ as precursor. However, the relative compositions of Pt and V were found to be somewhat lower in the case of $Fe(acac)_2$ than the use of $Fe^0(CO)_5$ as precursor. This observation likely suggests the possibility of a lower conversion efficiency for the reduction of $Fe(acac)_2$, in comparison with the efficiency in the thermal decomposition reaction of $Fe(CO)_5$. This assessment is supported by the fact that an increased amount of reducing agent was needed for the reduction reaction in the case of using $Fe(acac)_2$ as the precursor. In general, we conclude that the three synthesis conditions can effectively produce the desired nanoparticle sizes and compositions according to the synthetic parameters in terms of concentrations and feed ratios, but the exact composition in the ternary nanoparticles depends on the choice of the metal precursors.

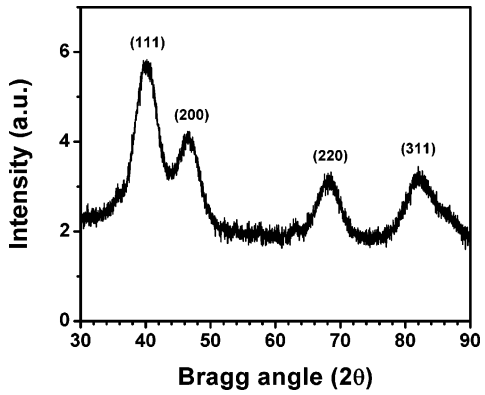

Figure 4. XRD powder spectrum for $Pt_{33}V_{14}Fe_{53}$ nanoparticles.

To investigate whether the ternary nanoparticles are simple aggregation of individual metal particles or an alloy of the individual metals, we used XRD technique to probe the crystallinity and size of the nanocrystals. Figure 4 shows a representative XRD spectrum for $Pt_{33}V_{14}Fe_{53}$ nanoparticles. This sample was prepared by dispersing the particles on carbon black support materials. The XRD data revealed a typical fcc pattern with some insignificant features indicative of chemically disordered structure. The calcination treatment of the nanoparticles led to rearrangement of Pt, V, and Fe atoms in the nanoparticles into long-range chemically ordered fcc structure. The formation of the alloyed nanocrystalline cores is supported by the fact that the diffraction peaks of metallic platinum shift to higher angles due to lattice shrinking resulting from the doping of smaller vanadium and iron atoms.[38] Indeed, the diffraction peak position falls between those for the monometallic Pt and those for monometallic V and Fe. For example, the strongest peak for Pt appears at $2\theta = 40.5$, slightly higher than Pt(111) peak ($2\theta = 39.8$).[37] Diffraction peaks corresponding to the strongest V(110) ($2\theta = 42.2$) and Fe (110) ($2\theta = 44.7$) known in the literature are apparently insignificant in the spectrum. We also know that the (111) peak for PtFe alloy nanoparticles appears at $2\theta = 41.2$, [30] which is not detected in the spectrum, suggesting the absence of PtFe nanoparticles in our PtVFe nanoparticles.

The average size of the nanoparticles was also estimated utilizing the Scherrer correlation shown in the following equation,

$$\Delta s = \frac{0.9}{D}$$

where

$$s = \frac{2(\sin\theta)}{\lambda} \qquad (1)$$

This equation relates the particle diameter (D) with the peak width (Δs, full width at half-maximum, $\lambda = 0.154$ nm) for Bragg diffraction from ideal single domain crystallites.[37] The calculated D value (1.4 nm) is very close to the value determined from TEM data (1.9 ± 0.3 nm). The remarkably close match of the TEM and XRD data supports that the ternary nanoparticles are largely alloyed in character.

(3) Structural Characterization of Capping Shells. Both FTIR and TGA techniques were used to characterize the structural properties of the encapsulating shells. The former provides qualitative information on the structures of the molecules capped on the surface of the nanocrystal cores, whereas the latter provides quantitative information on the relative core−shell composition.

Table 3. Summary of the Diagnostic FTIR Bands (cm^{-1}) for $Pt_{22}V_{35}Fe_{43}$ Nanoparticles, Oleylamine, and Oleic Acid

mode assignment	$Pt_{22}V_{35}Fe_{43}$ nanoparticles	oleylamine	oleic acid
$\nu_a(CH_3)$	∼2953	∼2953	∼2953
$\nu_s(CH_3)$	∼2872	∼2872	∼2872
$\nu_a(CH_2)$	2924	2924	2925
$\nu_s(CH_2)$	2853	2853	2854
ν(COOH)	1714		1712
$\nu(NH_2$ and $NH_3^+)$	1626	1580−1650	
$\nu_a(CO_2^-)$	∼1560		
$\nu_s(CO_2^-)$	1465	1465	1465

FTIR. Figure 5 shows a representative set of FTIR spectra, comparing the spectral characteristics for oleylamine, oleic acid, and (oleylamine/oleic acid)-capped PtVFe nanoparticles in both high- and low-frequency regions. The observed diagnostic bands are summarized in Table 3. The comparison of the spectral characteristics in the low-frequency region provides diagnostic information. The diagnostic bands include the band at 1712 cm^{-1} for the carbonyl stretching mode of $-CO_2H$ in oleic acid, the bands in 1580−1650 cm^{-1} for $-NH_2$ (and $-NH_3^+$) bending mode in oleylamine, and the bands at ∼1560 and ∼1465 cm^{-1} for the asymmetric and symmetric stretching modes of $-CO_2^-$ as well. In comparison with the observed bands of $-CO_2H$ (and possible $-CO_2^-$) for oleic acid and bands of $-NH_2$ (and possible $-NH_3^+$) for oleylamine, the observation of the bands at 1714, 1626, 1560, and 1465 cm^{-1} in the PtVFe nanoparticle sample indicates that the capping monolayer shell consists of both oleylamine and oleic acid.

In the high-frequency region, the overall similarity suggests the similar monolayer structures due to the similarity of hydrocarbon chains between oleylamine and oleic acid. The C−H stretching region provides the diagnostic information about the ordering properties of the chains. The bands corresponding to methyl stretching appear at 2953 and 2872 cm^{-1}, and the bands corresponding to the asymmetric and symmetric methylene stretching bands appear at 2925 and 2853 cm^{-1}. The slightly higher wavenumbers (5−8 cm^{-1}) for the methylene stretching bands than those observed for highly ordered or crystalline-like alkyl chains (2917 and 2848 cm^{-1}) on planar or large-sized metal particles[41] is characteristic of monolayer packing on smaller-sized particles,[41−45] similar to alkanethiolate monolayers on 2-nm sized gold nanoparticles.[41] The detection of the band at 3002 cm^{-1} is indicative of C−H stretching next to C═C, which is consistent with the presence of the structural unit in both

(41) Maye, M. M.; Zheng, W. X.; Leibowitz, F. L.; Ly, N. K.; Zhong, C. J. *Langmuir* **2000**, *16*, 490.
(42) Hostetler, M. J.; Stokes, J. J.; Murray, R. W. *Langmuir* **1996**, *12*, 3604.
(43) Hostetler, M. J.; Wingate, J. E.; Zhong, C. J.; Harris, J. E.; Vachet, R. W.; Clark, M. R.; Londono, J. D.; Green, S. J.; Stokes, J. J.; Wignall, G. D.; Glish, G. L.; Porter, M. D.; Evans, N. D.; Murray, R. W. *Langmuir* **1998**, *14*, 17.
(44) Nuzzo, R. G.; Dubois, L. H.; Allara, D. L. *J. Am. Chem. Soc.* **1990**, *112*, 558.
(45) Walczak, M. M.; Chung, C. K.; Stole, S. M.; Widrig, C. A.; Porter, M. D. *J. Am. Chem. Soc.* **1991**, *113*, 2370.

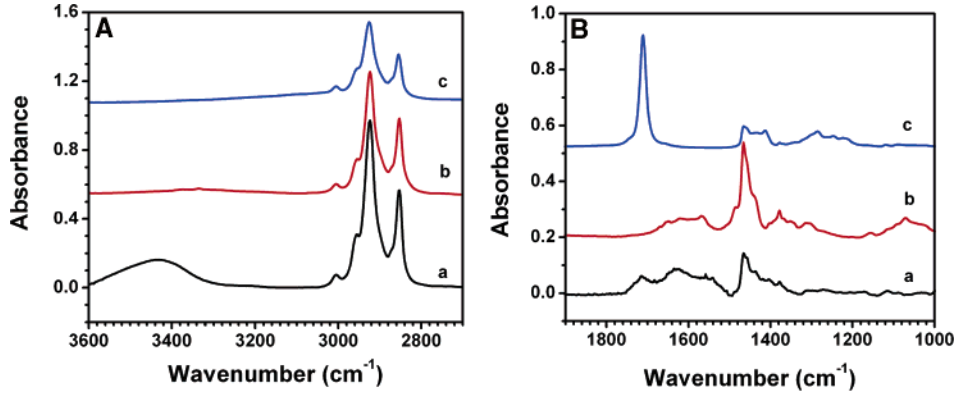

Figure 5. FTIR spectra in the high (A) and low (B) frequency regions for (oleylamine/oleic acid)-capped $Pt_{22}V_{35}Fe_{43}$ nanoparticles (a), oleylamine (b), and oleic acid (c).

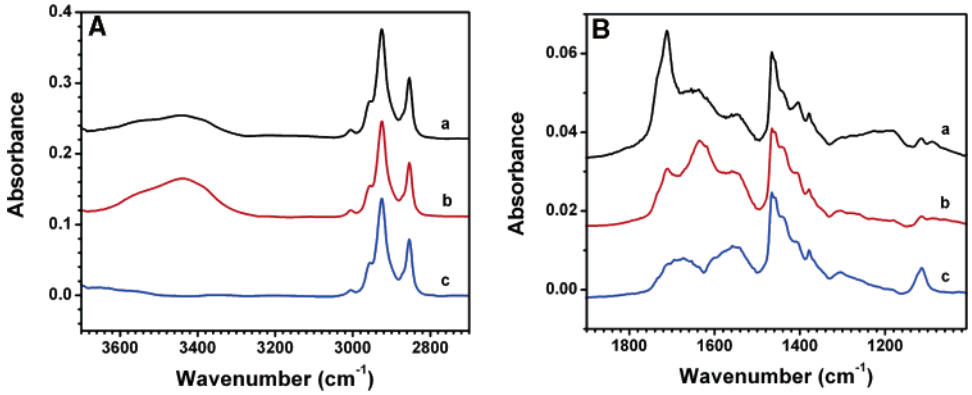

Figure 6. FTIR spectra in the high (A) and low (B) frequency regions for (oleylamine/oleic acid)-capped PtVFe nanoparticles of three different compositions. (a) $Pt_{29}V_{35}Fe_{36}$; (b) $Pt_{37}V_{16}Fe_{47}$; (c) $Pt_{32}V_{13}Fe_{55}$.

oleylamine and oleic acid. In the higher frequency region of ~3400 cm^{-1}, the possible presence of water in the nanoparticle samples prevented us from making unambiguous assignments about the N−H stretching bands of oleylamine.

In Figure 6, the spectral characteristics were further compared between PtVFe nanoparticles of three different compositions, $Pt_{29}V_{35}Fe_{36}$ (a), $Pt_{37}V_{16}Fe_{47}$ (b), and $Pt_{32}V_{13}Fe_{55}$ (c). While the spectral characteristics in the C−H stretching region (2800−3200 cm^{-1}) are essentially identical, there are clear differences in regions corresponding to bands of $-CO_2H$, $-CO_2^-$, $-NH_2$, and $-NH_3^+$ groups. We believe that the spectral difference reflects the difference in relative composition of the capping oleylamine and oleic acid molecules on the surface as a result of the difference in surface composition of the different nanocrystals. It appeared that the relative high concentration of Pt in the nanocrystal attracted more oleylamine, whereas the relative high concentration of V or Fe attracted more oleic acid in the mixed monolayer. While a more quantitative assessment of the relative shell composition is ongoing, the TGA data in the next subsection provided additional information for an indirect correlation of the core−shell composition.

TGA. Figure 7 shows a typical set of TGA data for PtVFe nanoparticles of two different compositions, $Pt_{37}V_{16}Fe_{47}$ (a) and $Pt_{32}V_{13}Fe_{55}$ (b). The TGA data show that the organic monolayer shell can be completely removed at ~300 °C. There is a 3−15% weight loss observed at ~100 °C, which is attributed to the loss of water in the samples.

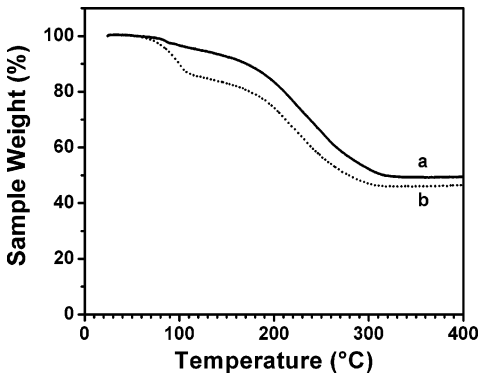

Figure 7. TGA curves obtained for (oleylamine/oleic acid)-capped nanoparticles of two different compositions: (a) $Pt_{37}V_{16}Fe_{47}$, (b) $Pt_{32}V_{13}Fe_{55}$ (heating rate 5 °C/min).

The loss of organic materials can be determined by subtracting the water loss from the total weight loss. It is estimated that 49% (a) and 47% (b) of organic component is being removed from $Pt_{37}V_{16}Fe_{47}$ (a) and $Pt_{32}V_{13}Fe_{55}$ (b) nanoparticles, respectively. On the basis of the TGA data, the percentage of organic capping shell in the $Pt_{33}V_{14}Fe_{53}$ nanoparticles could be estimated on the basis of a spherical model for the core−shell nanoparticle. For a spherical nanoparticle with a core size of 1.9 nm, the approximate number of metal atoms in the nanoparticle is ~250, and the approximate number of alkyl chains in densely packed monolayer assembly on the surface of the nanoparticle is ~80.[43] Using the above model and the average atomic weight (*AW*) for $Pt_{33}V_{14}Fe_{53}$ ($AW_{avg} = n1(Pt)\% \times AW(Pt) + n2(V)\%$

$\times$ *AW*(V) + *n3*(Fe)% $\times$ *AW*(Fe) = 0.33 $\times$ 195 + 0.14 $\times$ 50.9 + 0.53 $\times$ 55.8 = 101), the organic mass fraction for a full monolayer coverage of oleylamine or oleic acid on the nanocrystal surface was estimated. The calculation yields 46% (=(267 $\times$ 80)/(267 $\times$ 80 + 101 $\times$ 250)) and 47% (=(282 $\times$ 80)/(282 $\times$ 80 + 101 $\times$ 250)) for a full monolayer coverage of oleylamine and oleic acid, respectively. The above results indicate that the core−shell nanoparticles consist of 46−47% of organic weight in average, which is quite close to the weight percentage determined from the TGA data (47−49%).

Conclusion

We have demonstrated a size- and composition-controllable core−shell synthesis protocol for the preparation of ternary PtVFe nanoparticles. By manipulating the relative concentrations of the metal precursors, the protocol produces PtVFe nanoparticles with an average size of 1.4−3.5 nm and controlled ternary composition. The PtVFe nanoparticles synthesized were shown to be not only composition-controllable but also highly monodispersed. The ternary composition found in the nanoparticles can be correlated with the composition of the metal precursors used for the synthesis. The increase of Pt% in feeding ratio leads to an increase in Pt% in the nanoparticles. The V% found in the nanoparticles showed an indication of decrease in comparison with that used in the synthetic feeding, whereas the Fe% found in the nanoparticles was generally quite close to that used in the synthetic feeding. The formation of each metal in the alloyed nanocrystalline cores is dependent on the thermodynamic competition of the metal precursors in the chemical reduction, decomposition, and aggregation processes. The exact composition in the ternary nanoparticles also depends on the choice of the metal precursors. The core−shell nanoparticles contain a 47−49% mixture of oleylamine and oleic acid as the capping monolayer shell. The relative high concentration of Pt in the nanocrystal core appears to lead to more oleylamine, whereas the relative high concentration of V or Fe leads to more oleic acid in the mixed monolayer. Furthermore, the PtVFe nanoparticles have been shown to be easily assembled on carbon support materials with controllable dispersion and mass loading to produce the desired alloy composition. The carbon-supported alloy nanoparticles after calcination treatment were found to display high electrocatalytic activities for oxygen reduction in our recent work. The detailed results of these studies will be reported elsewhere, along with their implications to potential applications in fuel cell catalysts.

Acknowledgment. This work was supported by Honda Research Institute USA, Inc. We also thank Mr. H. H. Eichelberger (Department of Biology, SUNY-Binghamton) for assistance in TEM measurement, and Dr. H. R. Naslund (Department of Geological Sciences, SUNY-Binghamton) for assistance in DCP-AES analysis.

CM0508219